



OPEN Influence of foam content on mechanical properties and thermal conductivity of ceramsite foam concrete

Jing Zhang^{1,4}, Yuxin Su¹, Yudong Xiong³, Jianming He³, Qianyi Xu^{2✉} & Hongshuai Gao^{1✉}

Ceramsite foam concrete (CFC) is an innovative lightweight building material formulated by integrating ceramsite into foam concrete. It retains the inherent advantages of foam concrete while mitigating high drying shrinkage and excessive water absorption, significantly enhancing durability and compressive strength. This study investigates the effects of foam content on CFC's dry density, compressive strength, water absorption, softening coefficient, and thermal conductivity. The phenomena observed during the compression testing of the CFC specimens were also documented to analyze the degree of spalling. A novel predictive model for determining the thermal conductivity of CFC was originally developed and validated in this study. Results reveal strong linear relationships, foam content negatively correlates with density, strength, and softening coefficient, but positively correlates with thermal conductivity and water absorption. Increasing foam content also enlarges average pore size. These findings provide a theoretical foundation for optimizing CFC in energy-efficient building applications, offering significant potential for reducing energy consumption and improving thermal insulation in modern construction.

Keywords Foam concrete, Ceramsite, Mechanical properties, Thermal conductivity

In recent years, the continuous rise in global energy consumption has underscored the significance of energy-saving and environmentally friendly materials in practical applications, making it a prominent research focus¹. The advancement of eco-friendly, low-carbon, and energy-efficient materials is becoming an unavoidable direction in the future of building materials^{2,3}. The construction industry's demand for new materials is continuously increasing. These materials must possess excellent physical and chemical properties and be environmentally friendly in their production and use. Foam concrete is an innovative energy-saving and environmentally friendly material. It not only meets modern construction requirements but also offers significant potential for sustainable development in the construction industry.

Foam concrete finds wide application in the construction field because of its lightweight, insulating, soundproof⁴, fire-resistant, earthquake-resistant, durable, waste-utilizing, and environmentally friendly characteristics⁵. Additionally, foam concrete has the advantages of low cost, strong durability, a simple production process, and the capability of on-site casting⁶. Therefore, foam concrete has been extensively researched over the past twenty years^{7–9}, yielding substantial results. However, due to its high porosity, foam concrete is prone to significant drying shrinkage, cracking¹⁰, low strength, and high water absorption, which limits its widespread application. To overcome these performance limitations, researchers have explored methods to enhance foam concrete by adding lightweight aggregates. Research has demonstrated that lightweight aggregates can stabilize the internal structure of foam concrete¹¹. Additionally, different types of lightweight aggregates exert varying effects on the performance of foam concrete¹². The use of ceramsite and expanded perlite as lightweight aggregates in foam concrete offers a strong anchoring effect due to their rough surfaces. This reduces the dry density of the foam concrete and helps alleviate shrinkage issues¹³. When ceramsite is used as a lightweight aggregate and filling material, the physical and mechanical properties of foam concrete are significantly enhanced because the cement hydration products can penetrate the ceramsite, strengthening the bond between ceramsite and the cementitious material. In summary, the performance of foam concrete is significantly influenced by the type of

¹School of Civil Engineering, Heilongjiang University, Harbin 150080, China. ²College of Computer Science and Technology, College of Software, Heilongjiang University, Harbin 150080, People's Republic of China. ³Zhejiang Guangtian Component Group Co., Ltd., Ningbo 315000, China. ⁴Heilongjiang North Resilient City Research Institute, Harbin 150080, China. ✉email: xuqianyi@hlju.edu.cn; hongshuai.gao@hlju.edu.cn

Study	Research focus	Dry density (kg/m ³)	Compressive strength (MPa)	Thermal conductivity (W/(m·K))	References
Han et al. (2024)	Optimization of coal-based ceramsite in foam concrete	600–900	2.5–7.5 (28-day)	0.18–0.25	³
Wang et al. (2020)	Shrinkage and strength with coal gangue ceramsite	800–1200	4.0–10.0 (28-day)	–	¹¹
Schumacher et al. (2020)	Open structure and strength-to-density ratio	700–1000	3.0–8.0 (28-day)	0.20–0.30	¹³
Real et al. (2015)	Chloride migration and mechanical properties	900–1100	Reduced by 19.81–26.73%	–	²³
Liu et al. (2023)	Lightweight high-strength ceramsite aerated concrete	650–950	3.5–9.0 (28-day)	0.22–0.28	⁴²

Table 1. Comparison of existing studies on CFC.

Materials	CaO	SiO ₂	Al ₂ O ₃	Fe ₂ O ₃	MgO	SO ₃	TiO ₂	Cl ⁻	Loss
Cement/%	45.10	7.25	18.61	4.32	1.35	12.60	0.85	0.03	9.70
Fly ash/%	4.01	50.52	30.81	6.04	0.90	1.66	0.00	0.01	2.97

Table 2. Chemical composition of cement and fly ash.

lightweight aggregate used, and the use of ceramsite as a lightweight aggregate can effectively enhance its overall performance.

Ceramsite has found widespread application in the industrial sector due to its lightweight nature, high strength, and excellent chemical and thermal stability^{14,15}. In recent years, its use as a building material has expanded rapidly. For instance, ceramsite is increasingly used as a replacement for coarse aggregates in concrete, leading to the production of lightweight aggregate concrete, which achieves a weight reduction of about 25%¹⁶. Compared to traditional concrete, ceramsite-based lightweight concrete offers notable benefits, including improved insulation¹⁷, enhanced durability^{18–20}, and better seismic performance²¹. However, the inclusion of ceramsite can negatively impact the mechanical properties of the concrete, such as its tensile and compressive strength, as well as its elastic modulus²². Specifically, when ceramsite volumes of 250, 300, and 400 L/m³ are used, the compressive strength of the resulting concrete is reduced by 19.81%, 20.19%, and 26.73%, respectively²³. This decline is attributed to the lower mechanical properties of ceramsite compared to natural aggregate or even weaker than mortar. So the weakness is introduced into concrete and its mechanical properties are significantly reduced. Foam concrete, by nature, has significantly lower strength compared to mortar, and its strength is largely determined by its density²⁴. Therefore, carefully selecting the composition of foam concrete and ceramsite is essential to optimize their combined benefits, minimizing shrinkage while improving mechanical properties. Table 1 presents a comparison of studies on CFCs in existing literature.

In practical applications, the mechanical properties and thermal conductivity of CFC are of paramount importance. Excellent mechanical properties not only ensure the material's reliability in load-bearing and durability²⁵ but also effectively resist environmental stress²⁶ and long-term degradation. Foam content, as a critical variable, directly influences the overall performance of CFC^{27–29}. Current research on CFC primarily focuses on two aspects. Material composition optimization, studies aim to balance lightweight and strength by adjusting ceramsite-to-cement ratios³⁰. Single-property enhancement, most works isolate mechanical or thermal properties²³. Existing studies use limited foam content ranges, failing to establish full-spectrum relationships between foam content and multi-property performance. Few works correlate mesoscopic pore evolution with macroscopic mechanical and thermal conductivity properties. Current thermal conductivity models show > 20% error for CFC due to oversimplified pore assumptions.

This study utilizes foam content as a variable to prepare CFC, with the primary objective of investigating its impact on performance indicators such as dry apparent density, compressive strength, water absorption rate, softening coefficient, and thermal conductivity. Additionally, the study aims to establish linear relationships between foam content and each of these indicators, and to develop a thermal conductivity prediction model specifically tailored for CFC. By examining the influence of foam content on both the mechanical and thermal properties of CFC, this study seeks to address existing gaps in the literature and provide a comprehensive understanding, along with a predictive model for its thermal conductivity.

Experimental details

Raw materials

(1) Cement

The experiment utilized Grade 42.5 sulphoaluminate cement (SAC) from Nanjing Lepatai New Materials Technology Co. Ltd., with a specific surface area of 450 m²/kg. Compared to Portland cement, SAC has characteristics of crack resistance, rapid setting and hardening, and low volume change rate. According to standard GB/T 20472-2006, the chemical composition is shown in Table 2, and the morphology is shown in Fig. 1a.

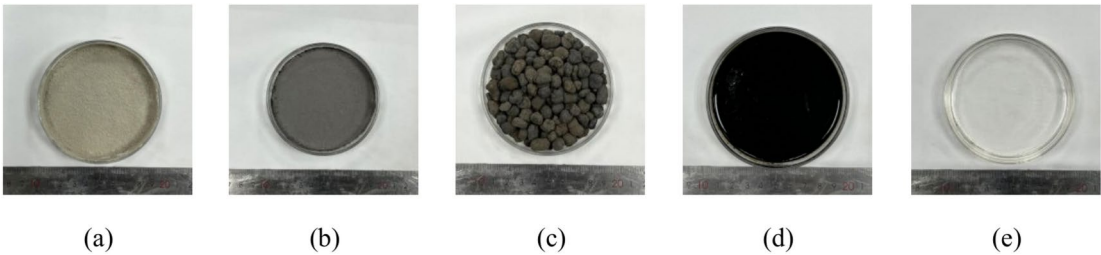


Fig. 1. Materials: (a) cement; (b) fly ash; (c) ceramsite; (d) foaming agent; (e) superplasticizer.

Cylinder compressive strength (MPa)	Bulk density (kg/m ³)	1 h water absorption rate (%)	Natural moisture content (%)	24 h water absorption rate (%)
1.5	350	10.5	4.25	12

Table 3. Performance of ceramsite.

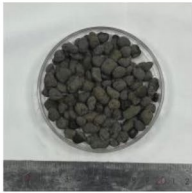



Main particle size(mm)	0~3.75	3.75~7.5	7.5~11.25	11.25~15
Ceramsite				
Proportion/%	6.1	22.7	60.3	9.2

Table 4. Particle size distribution of ceramsite.

(2) Fly ash

The experiment used Grade II fly ash produced by Ningbo Beilun Tianlu Building Materials Trading Co., Ltd., with an average particle size of 0.1–0.3 μm and a specific surface area of 20–28 m²/g. The chemical composition is shown in Table 2, and the morphology is shown in Fig. 1b.

(3) Ceramsite

The experiment used Grade 350 solid waste clay shale ceramsite produced by Jincai Building Materials Sales Co., Ltd. The physical and mechanical properties and particle size distribution are shown in Tables 3 and 4, and the morphology is shown in Fig. 1c. The water absorption and pore distribution are shown in Figs. 2 and 3. Figure 3 depicts the microscopic morphology of ceramsite, clearly revealing key features like surface and internal pores.

(4) Foaming agent

The experiment used TR-B composite polymer protein foaming agent produced by Luoyang Tongrun Information Technology Co., Ltd. The Foaming agent exhibited a foaming ratio of 25×, bleeding rate of 3.2%, and 1-h settlement ≤ 5 cm (tested per JG/T 266-2011). This product is a dark brown liquid, and its morphology is shown in Fig. 1d.

(5) Superplasticizer

The experiment utilized polycarboxylate superplasticizer produced by Chongqing Sika Chemical Group Co., Ltd., featuring a water reduction rate of 25%, a solid content of 39.7%, an air content of 3%, and a pH value of 6.1. The morphology of the superplasticizer is illustrated in Fig. 1e.

(6) Water

The experiment used tap water supplied by Ningbo Water Supply Co., Ltd. (Jiangdong Branch). The water source must be pollution-free and the water quality must be clean.

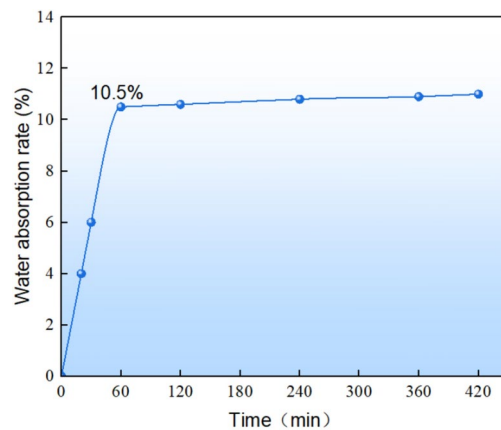


Fig. 2. Water absorption rate of ceramsite.

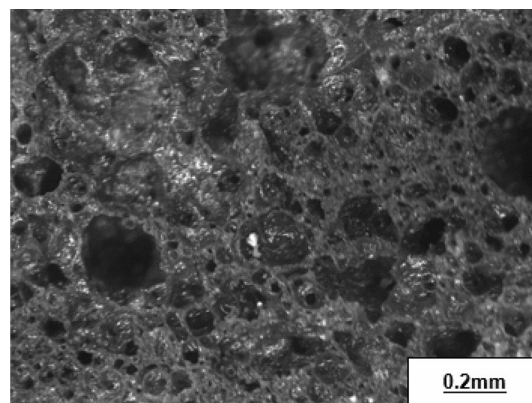


Fig. 3. Morphology of ceramsite.

Specimens	Cement (kg)	Fly ash (kg)	Ceramsite (kg)	Superplasticizer (kg)	Foam (L)	Water (kg)	Dry apparent density (kg/m ³)
CFC-01	400	70	235	1.33	2.5	105	1165
CFC-02	400	70	235	1.33	3	105	1050
CFC-03	400	70	235	1.33	3.5	105	977
CFC-04	400	70	235	1.33	4	105	915
CFC-05	400	70	235	1.33	4.5	105	830
CFC-06	400	70	235	1.33	5	105	760
CFC-07	400	70	235	1.33	5.5	105	691

Table 5. Mix proportions.

Mix proportions

The control variable method was utilized to investigate the mechanical properties and thermal conductivity of CFC with varying foam contents. According to the standard JG/T 2459-2018, seven groups of CFC with varying foam contents were designed using the physical foaming preparation process, with only the foam content being varied. The mix proportions are provided in Table 5. The quantity of water reducer utilized in the experiment was 0.3% of the cementitious material.

When the foam content exceeds 6L, the prepared CFC exhibits a dry apparent density of less than 660 kg/m³ and very low strength, leading to damage to the test blocks during demolding due to excessive foam content. Therefore, this experiment selected foam contents ranging from 2.5 to 5.5 L.

Preparation process

The preparation process of the specimen is shown in Fig. 4.

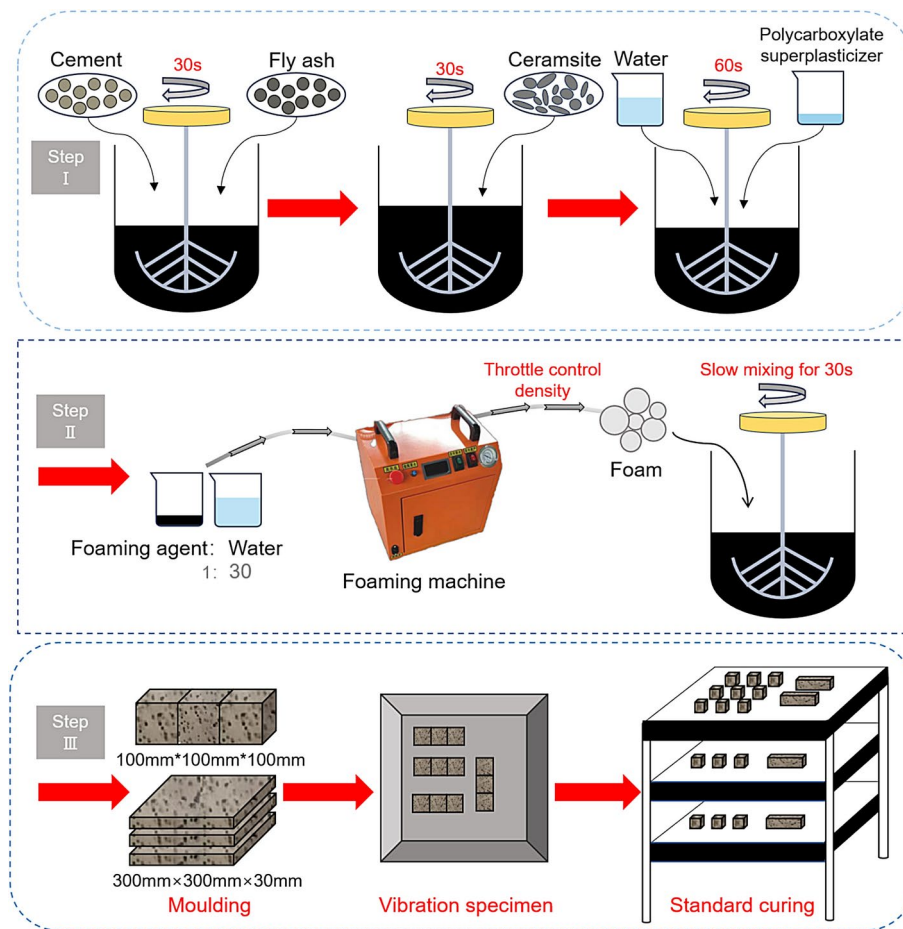


Fig. 4. Preparation process.

- (i). Pre-wet the ceramsite for 1 h, and prepare the foaming agent with water at a ratio of 1:30 for subsequent use.
- (ii). Weigh the required amounts of cement and fly ash according to the mix proportions, place them into a mixer, and mix for 30 s to ensure the powder is fully blended.
- (iii). Weigh the pre-wetted ceramsite, add it to the dry powder, and mix for 30 s until uniformly mixed.
- (iv). Add the specified amount of water and water reducer according to the mix proportions in Table 5 to obtain a mixture of ceramsite and cement slurry.
- (v). Use a foaming machine to prepare foam with a density of $50 (\pm 2)$ kg/m³, incorporate the appropriate amount of foam, and stir slowly for 30 s until the foam is fully integrated into the mixture.
- (vi). Pour the prepared slurry into molds of 100 mm × 100 mm × 100 mm and 300 mm × 300 mm × 30 mm, and vibrate on a vibrating table for 10 s to densify it. After vibrating, scrape off the excess slurry from the mold surface to smooth it.
- (vii). During the molding and demolding process, ensure the integrity of the test blocks and avoid surface damage. After 24 h, demold the test blocks and proceed with curing.

Selection of foaming agent

The foaming agent is a critical component in the preparation of CFC, with two primary methods: physical foaming and chemical foaming. Physical foaming involves incorporating pre-made foam into a mixture of cement slurry and ceramsite. The construction process is straightforward to execute. This experiment utilizes the physical foaming method. Common foaming agents include animal protein foaming agents, plant protein foaming agents, and composite protein foaming agents. These three foaming agents operate on the same principle but differ in foaming effectiveness. The foaming principle involves the degradation of proteins, where peptide bonds in large molecules break to form easily soluble protein molecules. As the concentration of protein molecules in the solution increases, hydrophobic groups gradually increase, reducing surface tension and forming interfaces. Specific groups within the molecules form hydrogen bonds. The strong hydrogen bonding ensures the solution forms a high-strength foam film, resulting in stable foam produced by the foaming agent.

To determine a suitable foaming agent, experiments were conducted to verify the foaming effectiveness of animal protein foaming agents, plant protein foaming agents, and composite protein foaming agents. The testing method provided by Yan Zhenjia et al.³¹ was employed due to its convenience. The steps are as follows:

- (i). Take an empty pure water bottle with no narrow waist and approximately the same thickness at the top and bottom. Use a syringe to draw 30 mL of pure water and inject it into the bottle.
- (ii). Take a 1 mL syringe used for skin tests in hospitals (graduated to 0.05 mL), draw 1 mL of the physical foaming agent to be tested, and inject it into 30 mL of water (diluted 30 times). Gently shake 3 times to mix the foaming agent with the water, minimizing bubble formation. Tighten the bottle cap.
- (iii). Hold the bottle with both hands, shake it vigorously up and down 30 times, then switch hands and shake it vigorously another 30 times. After the bottle is filled with foam, let it stand for 2 min and measure the foam height with a ruler. The height is the foaming height, used to assess the foaming ability.
- (iv). After 1 h, measure the foam height again and compare it with the previous height. The difference in height is the foam settlement distance, which can be used as a reference for foam stability. The larger the foam drop value, the poorer the quality.
- (v). To ensure accuracy, the above test should be repeated 3 times, and the average value should be taken.

The test results of the three foaming agents diluted 30 times are shown in Fig. 5. These results demonstrate that the plant-based protein foaming agent exhibits a relatively high foaming height, reaching 15.5 cm at 60 °C. However, its 1-h settlement distance is significant, measuring up to 12 cm, indicating poor foam stability. The animal protein foaming agent has the lowest foaming height and the smallest 1-h settlement distance, indicating better foam stability. The composite protein foaming agent has a moderate foaming height and the smallest 1-h settlement distance in the test, showing good performance in both foaming height and settlement distance. Therefore, the composite protein foaming agent was selected for the experiment.

Testing method

Dry apparent density test

After standard curing for 28 days, the CFC specimens were dried to a constant weight in an oven at 105 to 110 °C, with mass measured every 4 h. According to GB/T 17431.2-2010, when the mass change is within 1 g, the specimens are considered dried. The dry apparent density is calculated based on the volume and mass, with the average value taken. The specific operation is shown in Fig. 6a.

Compression test

The compressive strength of the dried CFC specimens is tested. During the test, the testing machine is first adjusted, the test platform is cleaned, and the specimen is positioned in the centre of the loading plate. The loading method is force-controlled, with a loading rate of 0.01 MPa/s, which is in accordance with the standard GB/T 50081-2019. This speed can ensure that the concrete specimens are uniformly stressed during the testing process, enabling the test results to accurately reflect their compressive strength performance and avoid test errors caused by too fast or too slow loading speeds. The failure process of the specimen is observed, and the pressure values and original stress–strain data are recorded. The specific operation is shown in Fig. 6b.

Water absorption and softening coefficient test

After cooling to room temperature, the specimens are placed in a constant temperature water bath at $(20 \pm 5)^\circ\text{C}$. According to GB/T 11969-2008, add water to 1/3 of the specimen's height and maintain for 24 h. Increase to 2/3 height and maintain for another 24 h. Then, cover the specimen with more than 30 mm of water and maintain for 24 h, as shown in Fig. 7. Remove the specimen, wipe off surface moisture, and immediately weigh it to the nearest gram. Calculate the water absorption rate using Eq. (1).

$$W_R = \frac{m_g - m_0}{m_0} \times 100 \quad (1)$$

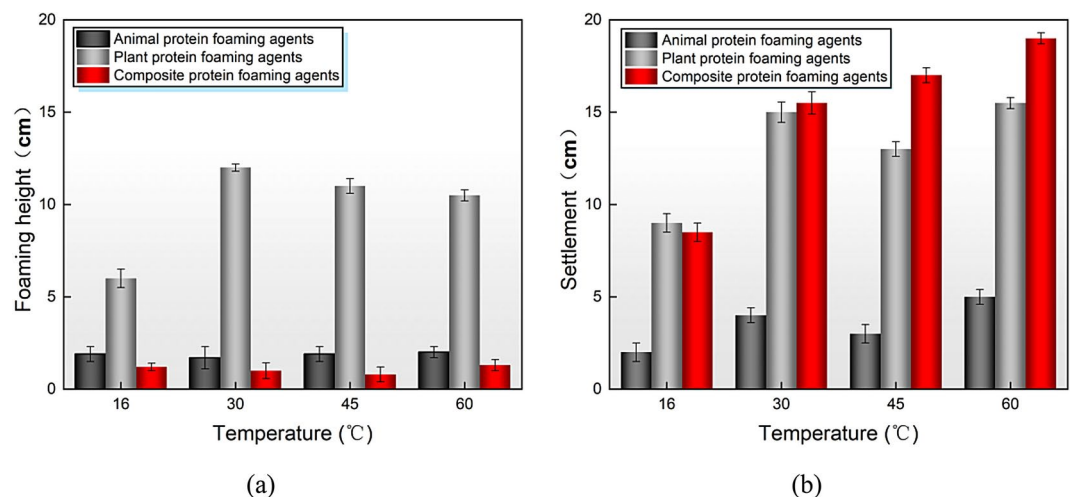


Fig. 5. Foaming effects: (a) foaming height; (b) settlement.

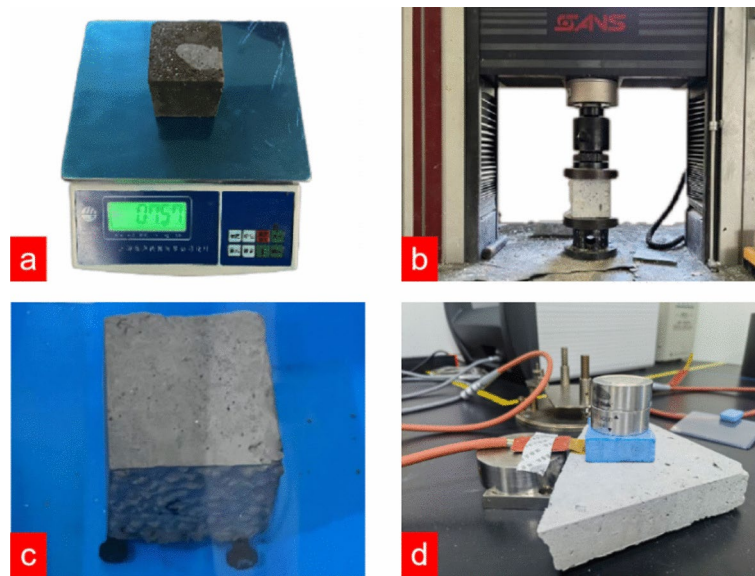


Fig. 6. Test methods: (a) dry apparent density test; (b) compressive strength test; (c) water absorption test; (d) thermal conductivity test.

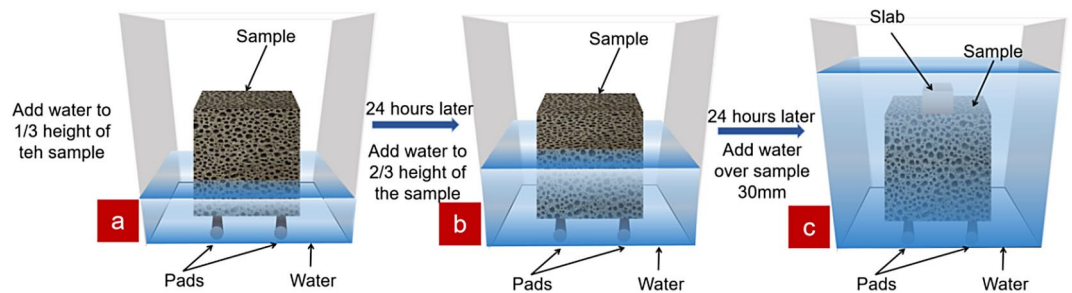


Fig. 7. Water absorption test procedure.

where W_R is the water absorption rate of the specimen, %. m_g is the mass of the specimen after water absorption, g. m_0 is the mass of the specimen after drying, g.

After soaking for 48 h, a compressive strength test was performed on the specimen to obtain the compressive strength of CFC in the saturated state. The ratio of the compressive strength in the saturated state to the compressive strength in the absolutely dry state is the softening coefficient of CFC, calculated according to Eq. (2).

$$\psi = \frac{f_1}{f_0} \quad (2)$$

where ψ is the softening coefficient of the specimen, f_1 is the compressive strength (saturated state), MPa. f_0 is the compressive strength (absolutely dry state), MPa.

The specific operation is shown in Fig. 6c.

Thermal conductivity test

Testing of the thermal conductivity of the dried CFC specimens used the Heson HS-DR-5 thermal conductivity meter based on the heat flow method. During the test, the specimen is placed in the specimen slot, and the specimen density (kg/m^3) and thickness (cm) are entered into the system software to measure the thermal conductivity. The thermal conductivity value is taken as the average of three specimens, with the test results accurate to $0.0001 \text{ W/(m}\cdot\text{K)}$. The environmental conditions ($20 \pm 2^\circ\text{C}$, $50 \pm 5\% \text{ RH}$) were selected based on GB/T 10294-2008 standard to minimize moisture-induced thermal resistance fluctuations and ensure measurement reproducibility. The specific operation is shown in Fig. 6d.

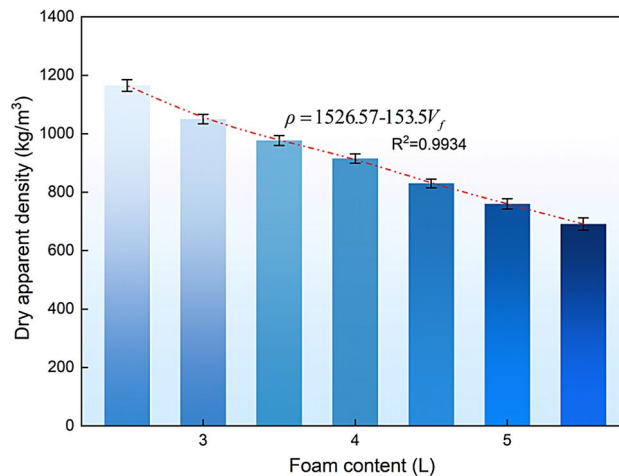


Fig. 8. Dry apparent density.

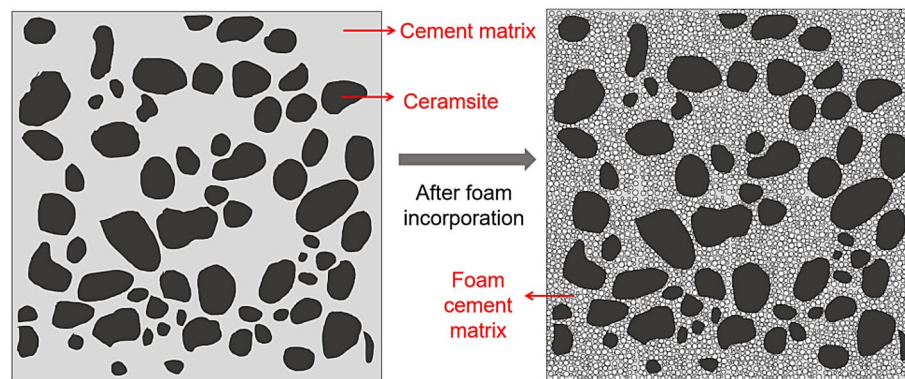


Fig. 9. Comparison before and after foam addition.

Results and analysis

Dry apparent density analysis

The test results of the dry apparent density of CFC are shown in Fig. 8. With the increase in foam content, the dry apparent density of CFC gradually decreases, showing a linear downward trend from 1165 to 691 kg/m³. By fitting the dry apparent density and foam content linearly, the result can be represented by Eq. (3).

$$\rho = 1526.57 - 153.5V_f \quad (3)$$

where ρ and V_f represent the dry apparent density and the foam content.

The density of the foam is 50 kg/m³, which is 1/40, 1/7, and 1/2 of the densities of cement, ceramsite and water, respectively, and is significantly lower than their densities. When foam is incorporated into the concrete, it forms corresponding bubble structures that displace an equivalent volume of slurry, occupying a certain volume and increasing the porosity of the concrete³². After curing, the foam creates a hollow structure, as illustrated in Fig. 9. As the foam content increases, the volume occupied by the foam increases, resulting in higher porosity and a lower dry apparent density.

Compression performance analysis

Experimental phenomena

Figure 10a illustrates the three stages of internal crack formation during the compression testing of the specimens. Initially, when the load is applied, cracks and pores compress, leading to the formation of a few internal cracks. As the load increases, cracks begin to propagate through the ceramsite in the CFC. Upon reaching peak load, both the ceramsite and foam concrete are crushed, concluding the test. Specimens from CFC-01 to CFC-07 exhibited varying degrees of spalling. Figure 10d, e show the final failure state of the test block during and after compression.

The failure modes are classified as matrix failure or ceramsite failure due to differences in the relative strengths of the foam-containing matrix and the ceramsite. Matrix failure occurs when the foam-containing matrix is crushed, while most of the matrix covering the ceramsite remains intact, meaning cracks primarily form and

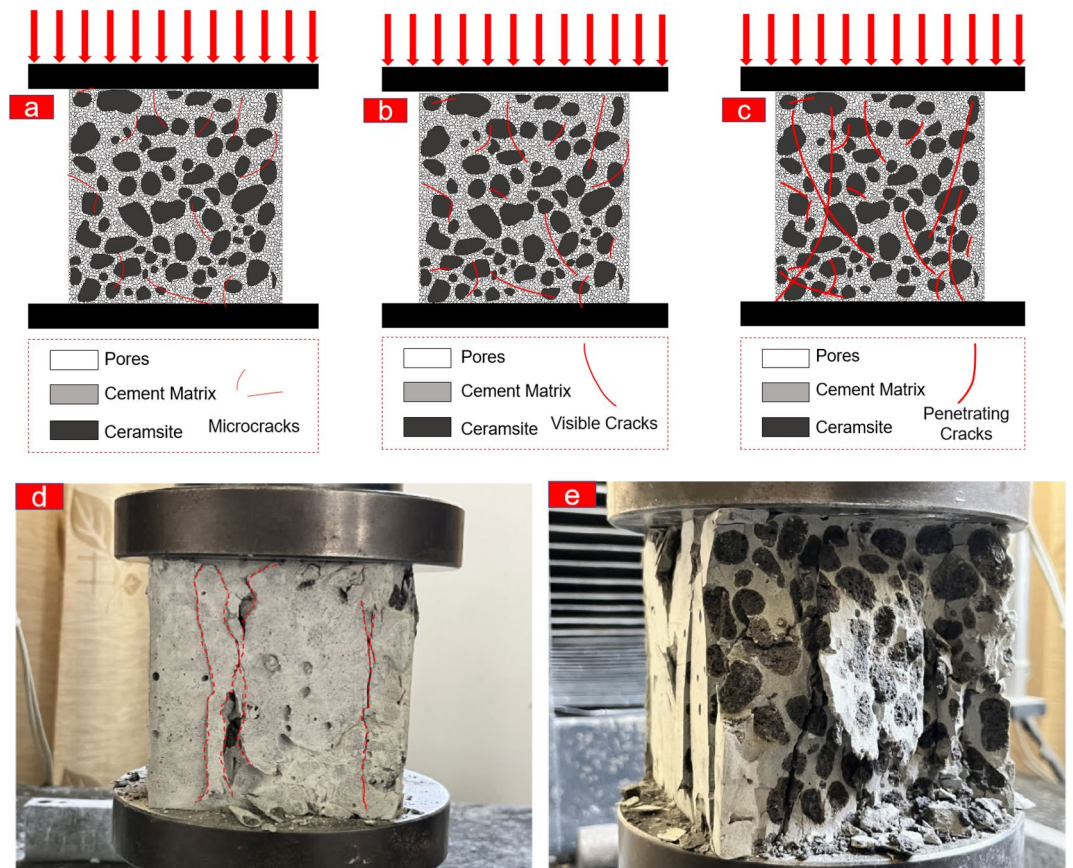


Fig. 10. CFC compression stages; (a) compression of cracks and pores; (b) crack initiation stage; (c) crack propagation stage; (d) specimen during compression process; (e) final failure state of specimen post-compression.

propagate within the matrix. Ceramsite failure is characterized by cracks propagating through the ceramsite, with both the ceramsite and matrix being crushed during the test. Increasing the density of the matrix enhances compressive strength.

When the matrix density is low, the dry apparent density of CFC ranges from 600 to 750 kg/m³, and its strength is correspondingly low. During compression, only the matrix is crushed, while the ceramsite particles remain intact, as illustrated in Fig. 11a. This scenario does not fully utilize the strength of the ceramsite, resulting in lower concrete strength and is classified as matrix failure.

When the matrix density is relatively high, the dry apparent density of CFC ranges from 900 to 1150 kg/m³, and the mechanical interlocking force between the concrete matrix and the ceramsite is sufficiently strong. During compression, both the ceramsite and the matrix are crushed. Here, the matrix strength exceeds the ceramsite strength, with the ceramsite introducing initial defects into the matrix, leading to what is classified as ceramsite failure, as depicted in Fig. 11b.

Both situations arise from the strength mismatch between the ceramsite and the concrete matrix. When the matrix density is optimal, the dry apparent density of CFC ranges from 750 to 900 kg/m³, exhibiting both ceramsite and matrix failure modes, as shown in Fig. 11c. This balance fully utilizes the compressive strength of both the ceramsite and matrix, achieving strength compatibility between them.

Compressive strength analysis

The compressive strength test results of CFC are presented in Fig. 12. As illustrated, with the increase in foam content, the 7-day, 14-day, and 28-day compressive strength of CFC gradually decreases. Among the seven groups, CFC-01, with a foam content of 2.5L, exhibits the highest compressive strength at 7, 14, and 28 days, with values of 6.72 MPa, 8.63 MPa, and 9.68 MPa, respectively. Conversely, CFC-07, with a foam content of 5.5L, shows the lowest compressive strength at 7, 14 and 28 days, with values of 0.96 MPa, 2.01 MPa, and 3.89 MPa, respectively. The 7-day, 14-day compressive strength was linearly fitted with foam content and dry apparent density, resulting in Eqs. (4)–(7), R² values are all greater than 0.9.

$$f_{7d} = 12.35 - 2.14V_f \quad (4)$$

$$f_{7d} = -0.0067\rho + 13.7234 \quad (5)$$

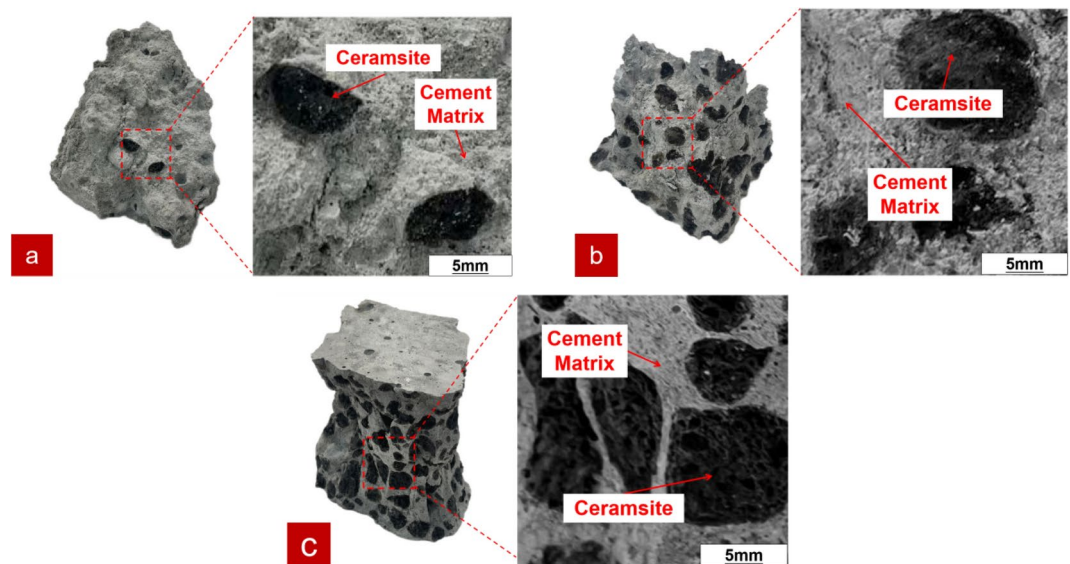


Fig. 11. Failure modes of CFC.

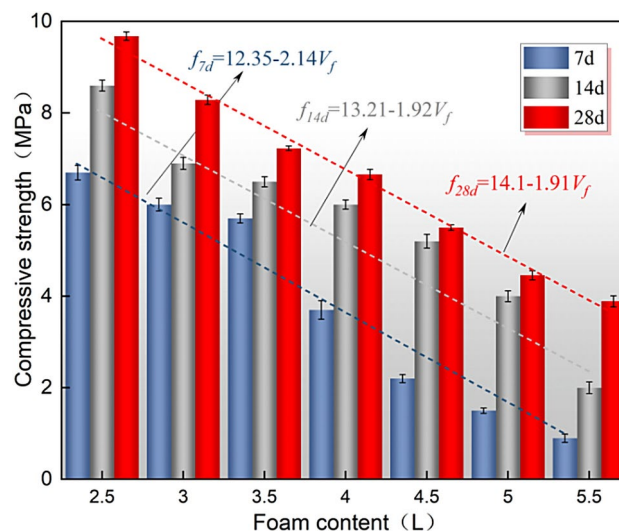


Fig. 12. Compressive strength.

$$f_{14d} = 13.21 - 1.92V_f \quad (6)$$

$$f_{14d} = -0.0087\rho + 17.80 \quad (7)$$

The 28-day compressive strength was linearly fitted with foam content and dry apparent density, resulting in Eq. (8) and Eq. (9) with R² values of 0.9897 and 0.9974, respectively, indicating a high degree of fit.

$$f_{28d} = 14.1 - 1.91V_f \quad (8)$$

$$f_{28d} = 0.01246\rho - 4.84 \quad (9)$$

The foam content affects the pore characteristics and material density, thereby influencing the compressive strength of CFC. The incorporation of foam introduces a substantial number of pores into the ceramsite concrete, resulting in internal material heterogeneity³³. This heterogeneity weakens the continuity and integrity of the solid material, leading to stress concentrations and the formation of weak areas with poor bonding in the interfacial transition zone (ITZ), ultimately reducing the compressive strength of the concrete.

Stress–strain curve

Figure 13a shows the stress–strain curves of CFC. Overall, the stress–strain curves of different CFC groups demonstrate similar patterns. In the elastic compression stage, the material undergoes elastic compression under pressure, and the stress increases linearly with strain. As loading continues and reaches a certain threshold, some weaker pore walls within the material begin to collapse, causing the material to undergo plastic deformation and become denser. During this phase, the stress remains constant. Subsequently, an elastic densification stage occurs, during which the stress increases with strain, showing a good linear relationship. At peak load, the material undergoes yield deformation and begins to fail, retaining some post-peak strength³⁴. From Fig. 13a, it is evident that CFC primarily exhibits top-down fracture failure.

Figure 13b illustrates the elastic modulus of CFC. It can be observed that as the foam content increases, the elastic modulus of CFC gradually decreases. Notably, the elastic modulus of CFC-07 is reduced by 28.2% compared to CFC-01. The increase in foam content leads to a decrease in the dry apparent density of the concrete and an increase in the pore structure, thereby reducing the elastic modulus of the concrete. By linearly fitting the elastic modulus with the foam content, Eq. (10) is derived, with an R2 value of 0.95135, indicating a good fit. E represents the elastic modulus.

$$E = 15.75571 - 1.109V_f \quad (10)$$

Degree of spalling

CFC is a multiphase composite material composed of ceramsite and foam cement slurry. During mixing and forming, concrete inevitably develops defects such as capillary pores and material cracks³⁵. When a load is applied to the concrete, internal stress is generated, restricting its volume change. Once the concrete experiences tensile stress exceeding its tensile strength, cracks will form in the specimen. As these cracks converge and propagate, the concrete will eventually be completely damaged. Therefore, the appearance of concrete after failure can directly reflect its mechanical properties³⁶.

Table 6 lists the degree of spalling for each group of specimens. (defined as the mass change of the specimen before and after the compressive test). The seven groups of specimens exhibited varying degrees of spalling. CFC-01 and CFC-02 specimens showed the smallest degree of spalling (16.5% and 23.5%, respectively). In these specimens, fine cracks were clearly observed, caused by internal micro-defects or stress concentration. The degree of spalling in CFC-03, CFC-04, and CFC-05 specimens was relatively moderate (26.1%, 29.4%, and 37.4%, respectively). CFC-04 exhibited diagonal shear cracks due to the action of shear forces, while in CFC-05, crack convergence points were noticeable. CFC-07 had the highest degree of spalling (50.3%), with longitudinal fractures.

The causes of these phenomena are as follows. The increase in foam content alters the internal microstructure of CFC. Higher foam content reduces the proportion of cement slurry, weakening the bond between the cement matrix and ceramsite, making the specimen more susceptible to cracking and spalling under load. Additionally, increased foam content enlarges the number and size of pores within the specimen, resulting in a coarser pore structure. This coarser pore structure makes the internal strength of the specimen more uneven, increasing the likelihood of cracking and spalling. Furthermore, higher foam content decreases the overall strength of the specimen, thereby increasing the probability of cracking and spalling. By linearly fitting the degree of spalling with the foam content, Eq. (11) is derived, with an R2 value of 0.97478, indicating a good fit.

$$S = -11.1571 + 10.87V_f \quad (11)$$

where S represents the degree of spalling, %.

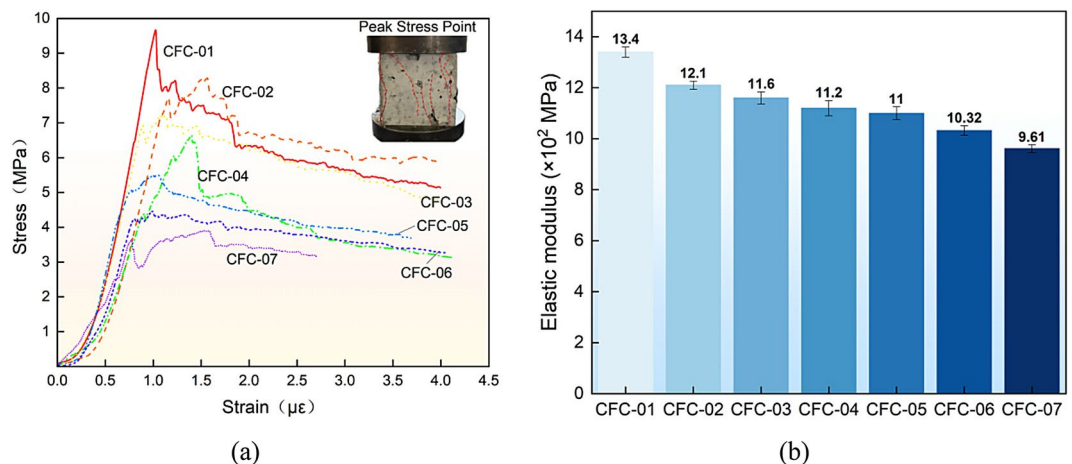
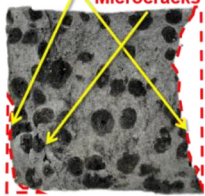
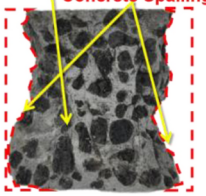
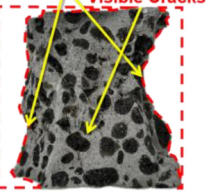
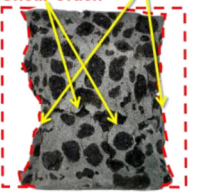


Fig. 13. Stress–strain analysis: (a) stress–strain curve; (b) elastic modulus.

Specimens	CFC-01	CFC-02	CFC-03	CFC-04
Spalling phenomenon				
Rate	16.5%	23.5%	26.1%	29.4%

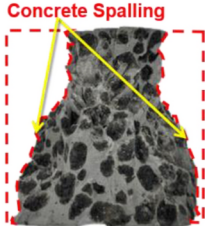
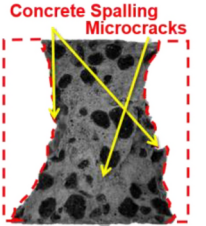

Specimens	CFC-05	CFC-06	CFC-07
Spalling phenomenon			
Rate	37.4%	42.8%	50.6%

Table 6. Spalling.

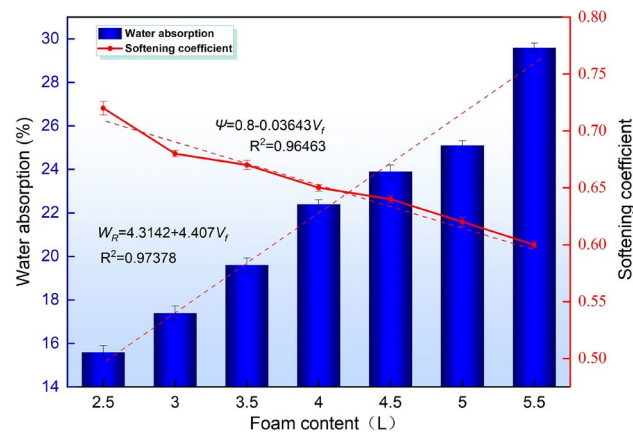


Fig. 14. Water absorption and softening coefficient.

Water absorption and softening coefficient test

As illustrated in Fig. 14, with the increase in foam content, the water absorption rate of CFC progressively rises, from 15% for CFC-01 to 29.6% for CFC-07. The softening coefficient gradually decreases, from 0.72 for CFC-01 to 0.6 for CFC-07.

The increased foam content reduces the proportion of the ceramsite cement matrix in the specimen, correspondingly increasing the number of bubbles and enhancing the connectivity of the material’s pore structure. This reduction in the saturated water absorption of the material in a waterlogged state decreases its resistance to external pressure and leads to a higher softening coefficient. Improved water resistance and stability of CFC can be achieved by reducing the foam content. Linear fitting of the water absorption rate and softening coefficient with the foam content yielded Eqs. (12) and (13), with R2 values of 0.97378 and 0.96463, respectively, indicating a good fit.

$$W_R = 4.3142 + 4.407V_f \tag{12}$$

$$\psi = 0.8 - 0.03643V_f \quad (13)$$

Thermal conductivity

The thermal conductivity test results of CFC are presented in Fig. 15. As the foam content increases, the thermal conductivity of CFC gradually decreases, exhibiting a linear downward trend. At a foam content of 2.5L, the thermal conductivity is the highest, approximately 0.29961 W/(m·K), while at a foam content of 5.5L, the thermal conductivity is the lowest, approximately 0.22942 W/(m·K). Between 2.5L and 5.5L foam content, the maximum reduction in concrete thermal conductivity is approximately 23.42%. By linearly fitting the thermal conductivity with the foam content, Eq. (14) is derived, with an R² value of 0.9682, indicating a good fit.

$$K = 0.3583 - 0.024V_f \quad (14)$$

The smaller the dry apparent density, the higher the proportion of pores in the foam concrete, and the lower the thermal conductivity of the material. The thermal conductivity of foam concrete is mainly influenced by the dry apparent density, and foam content is the primary factor directly affecting the dry density. Therefore, foam content is the main factor influencing the thermal conductivity of CFC.

Mesoscopic morphology

Between the microscopic scale of nanometers and the macroscopic scale of centimeters, there exists the mesoscopic scale of micrometers and millimeters. Concrete is considered a three-phase material composed of aggregates, cement, and the interfacial transition zone (ITZ) between them at the mesoscopic level³⁴. Additionally, the mechanical properties of concrete can be regarded as those of a mesoscopic homogeneous damage body. CFC with varying foam contents exhibits different cement matrix hardness and interfacial bond strength, which in turn affects the macroscopic mechanical properties of the concrete.

The significant difference between CFC and traditional concrete lies in its higher porosity³⁷. The structure and distribution of pores affect the various macroscopic properties of CFC³⁰. To elucidate the impact of pore structure characteristics on the macroscopic properties of concrete, the pore structure of CFC was binarized using Image Pro Plus 6.0 software. Based on the processed images, a statistical analysis of the pore structure parameters was conducted, resulting in the pore size distribution for different foam contents, as shown in Fig. 16.

As the sample density increases, the average pore size of CFC steadily increases. When the foam content is low, the pore size ranges from 150 to 250 μm, with a relatively compact pore structure. With a further increase in foam content, the pore size range expands to 250 μm to 350 μm, resulting in a looser pore structure and significantly larger pore sizes. This observation indicates that the increased filling degree of the cement matrix results in a denser microstructure of CFC.

The images also delineate certain areas to highlight the presence of internal defects within the pores. Lower-density concrete samples are typically associated with a higher incidence of inherent defects and internal damage within the pore network. These defects and damage negatively impact the mechanical properties of the concrete.

In the case of low foam content (CFC-01), the surface tension of the cement slurry is relatively high, resulting in the formation of primarily smaller pores. This small pore structure makes the internal pore network of the concrete more compact, enhancing its overall density. However, excessively high surface tension can also cause the pores to squeeze each other during formation, creating irregularly shaped pores, which can affect the overall uniformity and strength of the concrete.

As the foam content increases, the number and size of the pores increase significantly. Higher foam content reduces the surface tension of the cement slurry, facilitating the formation of larger pores. The shape of the pores becomes more regular, and their distribution more uniform, forming a more open pore network. This

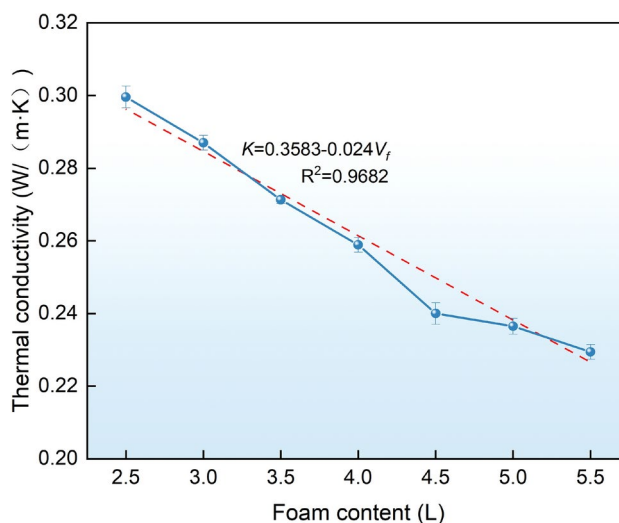
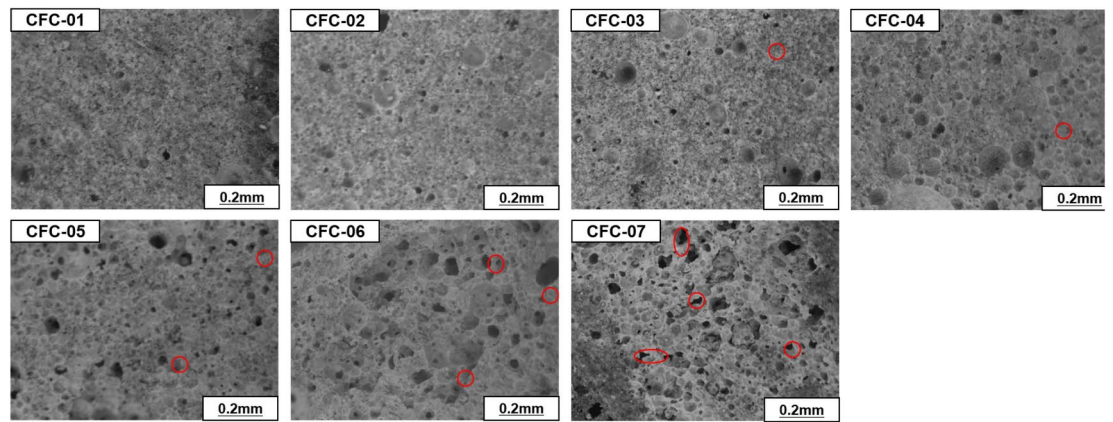
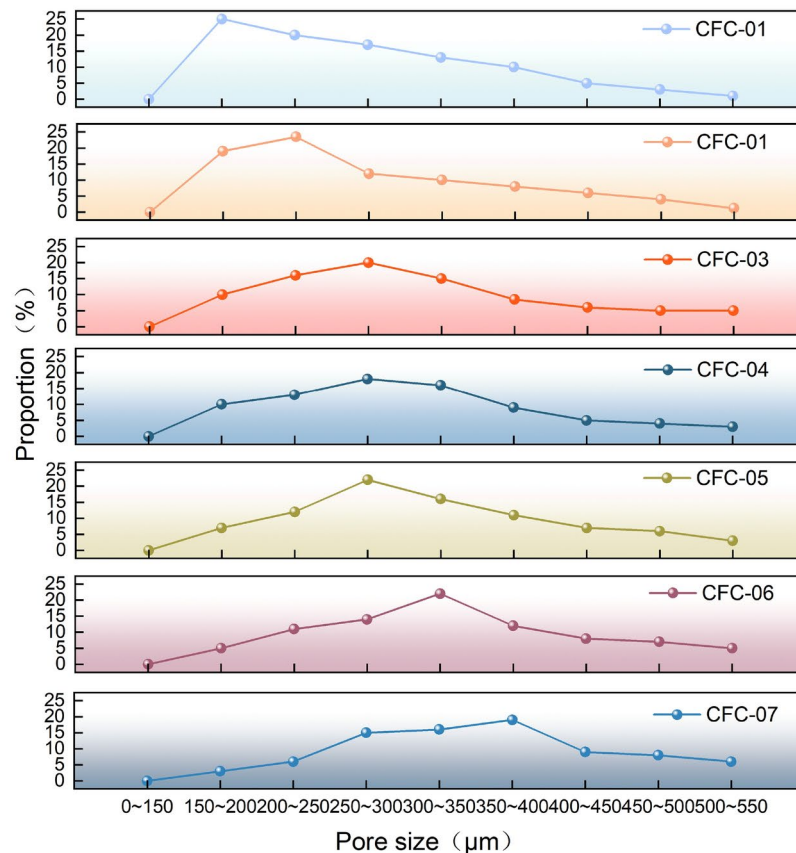


Fig. 15. Thermal conductivity.



(a)



(b)

Fig. 16. (a) Mesoscopic morphology, (b) pore size distribution.

change not only reduces the overall density of the concrete but also positively impacts its thermal and acoustic insulation properties. However, larger pores also mean that the mechanical strength of the concrete decreases, as the presence of pores reduces the effective load-bearing area, leading to a decrease in compressive strength.

Foam content has a significant impact on the pore structure and macroscopic mechanical properties of CFC. Properly adjusting the foam content can optimize the pore structure of the concrete, enhancing its physical and mechanical properties.

Thermal conductivity model of CFC

Model proposal

There are many models for calculating the apparent thermal conductivity of porous materials^{2,38–40}. However, even for the simplest two-phase porous materials, the discrepancy between the model's predictions and

experimental results is usually significant. Additionally, there is no unified model that can predict the thermal conductivity of different materials without adjustments. Cheng et al.⁴¹ improved upon Tsco's model and derived a new formula for calculating the thermal conductivity of two-phase materials—the Cheng-Vachon formula. This model assumes that the dispersed phase is randomly and uniformly distributed in the homogeneous phase. Through reasonable approximation, this distribution function can be expressed by the volume content of the dispersed phase. The analysis process begins with a cubic unit cell, which contains both dispersed and continuous phases, as illustrated in Fig. 17.

Based on the Cheng-Vachon model and incorporating the modified dispersed phase volume content introduced by Li Xiangyu et al., this study proposes an improved thermal conductivity model for CFC. The model was validated and refined by comparing it with experimental data.

The assumptions of the Cheng-Vachon formula include: the heat flow direction is parallel to the x-axis, heat convection and radiation are neglected, contact thermal resistance is ignored, the pores in the material are not considered, and the dispersed phase is uniformly distributed in the matrix. As shown in Fig. 17, the equivalent thermal resistance for this unit cell can be derived as:

$$R_e = 2 \int_0^x \frac{dx}{k_c + (k_d - k_c)y} + \frac{1 - 2x}{k_c} \quad (15)$$

where k_c is the thermal conductivity of the continuous phase (foam cement matrix), and k_d is the thermal conductivity of the dispersed phase (ceramsite).

The thermal conductivity of this unit cell is:

$$k_e = \frac{1}{R_e} \quad (16)$$

Assume the dispersed phase is uniformly and randomly distributed in the continuous matrix and follows the following normal distribution:

$$y = C_1 \exp(-C_2 x) = C_1 (1 - C_2 x^2 + \frac{C_2^2 x^4}{2!} - \dots) \quad (17)$$

Further simplification of Eq. (17) yields:

$$y = B + Cx^2 \quad (18)$$

In Eq. (18), B and C are constants, and the volume content of the dispersed phase can be calculated using Eq. (19):

$$\varphi = 2 \int_0^{1/2} y dx \quad (19)$$

By introducing boundary conditions, the expressions for B and C are obtained:

$$B = \sqrt{3\varphi/2} \quad (20)$$

$$C = -4\sqrt{\frac{2}{3}}\varphi \quad (21)$$

Substituting into Eq. (15) yields

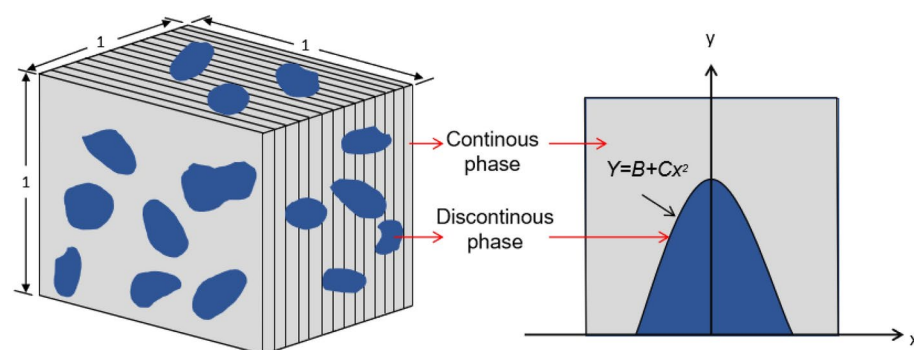


Fig. 17. Distribution of discontinuous phase in unit cell.

$$R_e = 2 \int_0^{B/2} \frac{dx}{[k_c + B(k_d - k_c)] - C'(k_d - k_c)x^2} + \frac{1 - B}{k_c} \tag{22}$$

In the derivation of the Cheng-Vachon formula above, from Eqs. (19) to (21), the maximum volume content of the dispersed phase is 0.667. When the dispersed phase volume content is large, the calculation results will be biased, especially for foam concrete, which often has a large dispersed phase volume content. Using the Cheng-Vachon formula to calculate the thermal conductivity of foam concrete results in significant errors. Li Xiangyu et al. proposed a correction Eq. for the volume content of the dispersed phase based on the Cheng-Vachon formula:

$$\varphi' = \varphi^{1/3} \frac{\frac{k_c}{k_d}^{1/3} - \varphi^{1/3}}{\frac{k_c}{k_d}^{1/3} - 1} \tag{23}$$

where φ represents the volume content of the dispersed phase, and φ' represents the corrected volume content of the dispersed phase.

According to this correction Eq., combined with Eq. (15), the equivalent thermal resistance of CFC is:

$$R'_e = \frac{\sqrt{\varphi'}}{k_c + (k_d - k_c)\sqrt{\varphi'}} + \frac{1 - \sqrt{\varphi'}}{k_c} \tag{24}$$

The thermal conductivity of CFC is the reciprocal of the thermal resistance:

$$k_e = \frac{1}{R'_e} \tag{25}$$

Model validation

Equation (25) is the thermal conductivity calculation model formula for CFC. This formula is used to calculate the thermal conductivity of the seven groups of specimens prepared in this study. The applicability of the formula is verified using the data from references³ and⁴². The thermal conductivity k_d can be obtained using Eq. (26)².

$$k_d = 0.0841 \times e^{0.001\rho} \tag{26}$$

where ρ is the apparent density of ceramsite in the dry state.

Combining k_c and k_d from Table 7 and the calculated φ' , substituting into Eq. (25) yields the calculated thermal conductivity values of the CFC in this study. The applicability is verified, and the results are shown in Fig. 18. It can be seen that 89% of the calculated results from the thermal conductivity model established in this study are within a 10% error margin compared to the experimental results, indicating small errors. The overall trend of the predicted results shows a certain degree of reference value.

Conclusions

This study systematically investigated the effects of foam content on ceramsite foam concrete (CFC) through experimental and analytical approaches. The research results are as follows:

- (1) The study produced seven distinct CFC mixtures with systematically varying foam contents. The resulting dry apparent densities ranged from 691 to 1165 kg/m³. The 28-day compressive strengths of the specimens varied between 3.89 and 9.86 MPa. Water absorption rates ranged from 15.6 to 25.6%, softening coefficients varied between 0.6 and 0.72, and thermal conductivities ranged from 0.2294 to 0.295 W/(m·K).
- (2) An increase in foam content led to a gradual reduction in dry apparent density, compressive strength, and softening coefficient. Conversely, thermal conductivity, water absorption rate, and spalling degree exhibited an increase, demonstrating a clear linear relationship with foam content.
- (3) Developed and validated a thermal conductivity prediction model specifically tailored for CFC. The model demonstrated a high degree of accuracy, 89% predictions within 10% error. This indicates minimal error and provides a valuable reference for future applications of CFC.

	k_c	k_d	φ'	k_e	Measured value	Proportion
1	0.3094	0.2613	0.556	0.2813	0.2996	0.94
2	0.2965	0.2613	0.605	0.2741	0.2870	0.96
3	0.2536	0.2613	0.641	0.2622	0.2713	0.97
4	0.2358	0.2613	0.652	0.2503	0.2589	0.97
5	0.2215	0.2613	0.686	0.2472	0.2352	1.05
6	0.2143	0.2613	0.710	0.2458	0.2365	1.04
7	0.1811	0.2613	0.723	0.2348	0.2294	1.02

Table 7. Formula values.

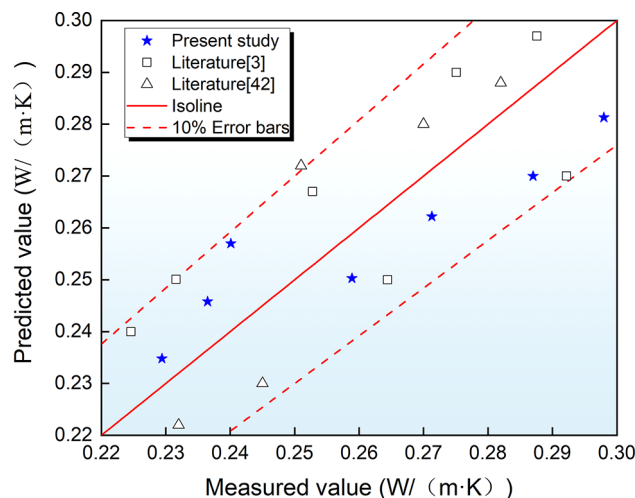


Fig. 18. Comparison of measured and predicted values.

(4) The average pore diameter of CFC increased progressively with higher foam content. Increasing foam content enlarged average pore size from 150–250 μm to 250–350 μm , transitioning from dense to loose microstructures.

CFC can be applied to different scenes by adjusting the foam content. Low foam content (2.5–3.5 L) suitable for structural thermal insulation composite wall requiring strength (6–10 MPa). High foam content (4.5–5.5 L) it is a pure thermal insulation layer suitable for roof/floor to maximize the thermal performance. This study provides the basis for the practical application of CFC in buildings and provides the potential for reducing building energy consumption. Future studies should focus on lifecycle assessment and large-scale durability testing to accelerate commercialization.

Data availability

Data will be made available on request. Please contact the corresponding author, Hongshuai Gao, for further details.

Received: 7 November 2024; Accepted: 28 April 2025

Published online: 15 May 2025

References

- Liu, J., An, S. & Zhang, Y. Mechanism of regulating the mechanical properties and paste structure of supersulfated cement through ultrafine iron tailings powder. *Cement Concr. Compos.* **140**, 105061 (2023).
- Real, S., Maia, C., Bogas, J. A. & Gomes, M. D. G. Thermal conductivity modelling of structural lightweight aggregate concrete. *Mag. Concr. Res.* **73**, 798–809 (2021).
- Han, Y., Zhou, M., Wang, J., Tian, Y. & Wang, X. Optimization of coal-based solid waste ceramsite foam concrete mix proportions and performance study. *Constr. Build. Mater.* **416**, 135226 (2024).
- Laukaitis, A. & Fiks, B. Acoustical properties of aerated autoclaved concrete. *Appl. Acoust.* **67**, 284–296 (2006).
- Ramamurthy, K., Kunhanandan Nambiar, E. K. & Indu Siva Ranjani, G. A classification of studies on properties of foam concrete. *Cement Concr. Compos.* **31**, 388–396 (2009).
- Jiang, J., Lu, Z., Niu, Y., Li, J. & Zhang, Y. Study on the preparation and properties of high-porosity foamed concretes based on ordinary Portland cement. *Mater. Des.* **92**, 949–959 (2016).
- Zhou, H., Jia, K., Wang, X., Xiong, M.-X. & Wang, Y. Experimental and numerical investigation of low velocity impact response of foam concrete filled auxetic honeycombs. *Thin-Walled Struct.* **154**, 106898 (2020).
- Nambiar, E. K. K. & Ramamurthy, K. Influence of filler type on the properties of foam concrete. *Cement Concr. Compos.* **28**, 475–480 (2006).
- Pokorný, J. et al. Bio-based aggregate in the production of advanced thermal-insulating concrete with improved acoustic performance. *Constr. Build. Mater.* **358**, 129436 (2022).
- Cao, D. et al. Effect of polyvinyl alcohol on the performance of carbon fixation foam concrete. *Constr. Build. Mater.* **390**, 131775 (2023).
- Wang, Y., Qiu, J. & Zeng, C. Shrinkage and strength properties of coal gangue ceramsite lightweight aggregate concrete. *Adv. Mater. Sci. Eng.* **2020**, 1–10 (2020).
- Gencel, O. et al. The effect of limestone and bottom ash sand with recycled fine aggregate in foam concrete. *J. Build. Eng.* **54**, 104689 (2022).
- Schumacher, K., Saßmannshausen, N., Pritzel, C. & Trettin, R. Lightweight aggregate concrete with an open structure and a porous matrix with an improved ratio of compressive strength to dry density. *Constr. Build. Mater.* **264**, 120167 (2020).
- Tong, L. et al. Sludge-based ceramsite for environmental remediation and architecture ingredients. *J. Clean. Prod.* **448**, 141556 (2024).
- Zhao, H. et al. Preparation of high-strength ceramsite via co-sintering of shield tunnel muck and steel slag: Correlation investigation on phase composition and particle strength. *Constr. Build. Mater.* **439**, 137413 (2024).
- Aslam, M., Shafigh, P., Alizadeh Nomeli, M. & Zamin Jumaat, M. Manufacturing of high-strength lightweight aggregate concrete using blended coarse lightweight aggregates. *J. Build. Eng.* **13**, 53–62 (2017).

17. Bogas, J. A. & Cunha, D. Non-structural lightweight concrete with volcanic scoria aggregates for lightweight fill in building's floors. *Constr. Build. Mater.* **135**, 151–163 (2017).
18. Jóźwiak-Niedźwiedzka, D. Scaling resistance of high performance concretes containing a small portion of pre-wetted lightweight fine aggregate. *Cement Concr. Compos.* **27**, 709–715 (2005).
19. Wang, H. Y. & Tsai, K. C. Engineering properties of lightweight aggregate concrete made from dredged silt. *Cement Concr. Compos.* **28**, 481–485 (2006).
20. Youm, K.-S., Moon, J., Cho, J.-Y. & Kim, J. J. Experimental study on strength and durability of lightweight aggregate concrete containing silica fume. *Constr. Build. Mater.* **114**, 517–527 (2016).
21. Real, S., Gomes, M. G., Moret Rodrigues, A. & Bogas, J. A. Contribution of structural lightweight aggregate concrete to the reduction of thermal bridging effect in buildings. *Construct. Build. Mater.* **121**, 460–470 (2016).
22. Sivakumar, S. & Kameshwari, B. Influence of fly ash, bottom ash, and light expanded clay aggregate on concrete. *Adv. Mater. Sci. Eng.* **2015**, 1–9 (2015).
23. Real, S., Bogas, J. A. & Pontes, J. Chloride migration in structural lightweight aggregate concrete produced with different binders. *Constr. Build. Mater.* **98**, 425–436 (2015).
24. Ma, Q., Shi, Y., Ma, D., Huang, K. & Yang, X. Effect of sludge ceramsite particle grade on static and dynamic mechanical properties of alkali-activated slag lightweight concrete at early age. *J. Build. Eng.* **69**, 106330 (2023).
25. Zhang, X. et al. Durability against dry-wet and freeze-thaw cycles of carbon sequestration foamed concrete utilizing abandoned soil and waste serpentine. *J. Build. Eng.* **95**, 110194 (2024).
26. Shafei, B., Alipour, A. & Shinozuka, M. Prediction of corrosion initiation in reinforced concrete members subjected to environmental stressors: A finite-element framework. *Cem. Concr. Res.* **42**, 365–376 (2012).
27. Shi, X., Ning, B., Na, F., Zhao, W. & Zhang, C. Study on properties of re-dispersible latex powder and polypropylene fiber-reinforced lightweight foam concrete. *J. Build. Eng.* **95**, 110156 (2024).
28. Zhang, C., Fan, D., Lu, J.-X., Pang, C. & Poon, C. S. Ultra-stable foam enabled by nano silica engineering for foam concrete improvement. *Cement Concr. Compos.* **150**, 105575 (2024).
29. Xiong, Y., Zhang, Z., Zhang, C. & Xiao, J. Foam-stability enhancement in biochar-infused foam concrete: Analyzing ionic strength, interparticle distance, and water state. *J. Clean. Prod.* **443**, 141231 (2024).
30. Mohamed, A. M., Tayeh, B. A., Majeed, S. S., Aisheh, Y. I. A. & Salih, M. N. A. Ultra-light foamed concrete mechanical properties and thermal insulation perspective: A comprehensive review. *J. CO2 Utiliz.* **83**, 102827 (2024).
31. 闫振甲, 何艳君编著. 高性能泡沫混凝土保温制品实用技术. 331 (北京: 中国建材工业出版社, 2015).
32. Li, P. et al. Preparation and optimization of ultra-light and thermal insulative aerogel foam concrete. *Constr. Build. Mater.* **205**, 529–542 (2019).
33. Liu, C., Su, J., Li, Z., Luan, K. & Zhou, G. Study on the post-fire axial compressive performance of the lightweight ceramsite foamed concrete sandwich composite shear wall. *Structures* **58**, 105589 (2023).
34. Bin Ruan, Li, J., Gan, Y. & Huang, J. Mesoscopic simulation of the mechanical behaviour of foam concrete subjected to large compressive deformation. *Construct. Build. Mater.* **418**, 135367 (2024).
35. Duan, H., Liu, H., Li, B., Wang, Z. & Gao, H. Mechanical properties and mechanism analysis of graphite tailings environment-friendly concrete. *Materials* **15**, 8870 (2022).
36. Farnam, S. M. & Rezaie, F. Simulation of crack propagation in prestressed concrete sleepers by fracture mechanics. *Eng. Fail. Anal.* **96**, 109–117 (2019).
37. Bie, Y., Ba, S. & Chen, S. Studies on foamed concrete micropores and their effects on stress distribution and heat conduction. *J. Build. Eng.* **87**, 109152 (2024).
38. Li, X. *Investigations on Thermal Conductivity Models of Foamed Concrete*.
39. Cakiroglu, C., Batool, F., Islam, K. & Nehdi, M. L. Explainable ensemble learning predictive model for thermal conductivity of cement-based foam. *Constr. Build. Mater.* **421**, 135663 (2024).
40. Yang, Y., Wang, Y. & Cao, J. Prediction and evaluation of thermal conductivity in nanomaterial-reinforced cementitious composites. *Cem. Concr. Res.* **172**, 107240 (2023).
41. Cheng, S. C. & Vachon, R. I. The prediction of the thermal conductivity of two and three phase solid heterogeneous mixtures. *Int. J. Heat Mass Transf.* **12**, 249–264 (1969).
42. Liu, P. et al. Study on the preparation and performances analysis of lightweight high strength ceramsite aerated concrete. *J. Market. Res.* **25**, 6672–6683 (2023).

Acknowledgements

The authors acknowledge the financial support provided by fundamental scientific research expenses at Heilongjiang Provincial College and University (2022-KYYWF-1129, 2024-KYYWF-0076 and Heilongjiang Province Ecological Environment Protection Research Project (HST2023GF004) and Key laboratory of flood disaster risk warning and prevention and control, Ministry of Emergency Management (2024YJ007-003).

Author contributions

Jing Zhang led the entire research project, including experimental design, data collection and analysis. Yuxin Su provided key technical support during the experimental process and made significant contributions to the scientific interpretation and theoretical analysis of the experimental results, and was responsible for writing and revising the paper. Yudong Xiong was responsible for part of the experimental operations and contributed to the collection and preliminary processing of data. Jianming He participated in the experimental design and provided professional advice on material selection and determination of experimental methods. Qianyi Xu contributed to the literature review and the establishment of the theoretical framework, providing a theoretical basis for the research. Hongshuai Gao provided valuable comments and feedback during the writing process of the paper, contributing to the improvement of the paper's structure and content. All authors reviewed the manuscript.

Competing interests

The authors declare no competing interests.

Additional information

Correspondence and requests for materials should be addressed to Q.X. or H.G.

Reprints and permissions information is available at www.nature.com/reprints.

Publisher's note Springer Nature remains neutral with regard to jurisdictional claims in published maps and institutional affiliations.

Open Access This article is licensed under a Creative Commons Attribution-NonCommercial-NoDerivatives 4.0 International License, which permits any non-commercial use, sharing, distribution and reproduction in any medium or format, as long as you give appropriate credit to the original author(s) and the source, provide a link to the Creative Commons licence, and indicate if you modified the licensed material. You do not have permission under this licence to share adapted material derived from this article or parts of it. The images or other third party material in this article are included in the article's Creative Commons licence, unless indicated otherwise in a credit line to the material. If material is not included in the article's Creative Commons licence and your intended use is not permitted by statutory regulation or exceeds the permitted use, you will need to obtain permission directly from the copyright holder. To view a copy of this licence, visit <http://creativecommons.org/licenses/by-nc-nd/4.0/>.

© The Author(s) 2025